LA-UR-20-23767

Title:	Modeling Metallic Fuel using Peridynamics
Author(s):	Unal, Cetin Chen, Hailong
Intended for:	Report
Issued:	2020-05-20

Modeling Metallic Fuel using Peridynamics

Hailong Chen[*] and Cetin Unal[†]

ABSTRACT

This report is prepared to fulfill Los Alamos National Laboratory's (LANL) deliverable for the project entitled "Simulation of fuel fragmentation, relocation and ballooning through peridynamics in MOOSE framework" awarded by DOE Nuclear Energy University Program (NEUP). The work is performed by Hailong Chen who is assistant professor at University of Kentucky as principal investigator with participation and direction of Cetin Unal from LANL.

Based on available modeling and simulation capabilities of peridynamics module in MOOSE framework for oxide fuel, the overall goal of this project is to further develop the peridynamics capabilities for modeling metallic fuel. It includes two major tasks: 1) develop validated scheme to handle the shape tensor singularity due to insufficient active neighbors of a material particle in the peridynamic correspondence model for fracture problems, and 2) develop failure modeling scheme including failure criterion for metallic fuels.

Before the peridynamics can be applied to model metallic fuel, the formulation instability of the peridynamic correspondence model should be addressed. The PI first worked on developing new stabilization method to improve the performance of the peridynamic correspondence model and reduce the possibility of getting a singular shape tensor while applying the model for fracture problems. The new stabilization scheme uses bond-associated weight function rather than bond-associated horizon. Compared to bond-associated horizon stabilized method, this new stabilization scheme has better performance with improved prediction accuracy and reduced free surface effect. Using this newly developed stabilization, materials models from BISON can be directly used in peridynamics for metallic fuels, such as fission rate and burnup dependent creep and swell models. Publication of this work is under preparation.

To address issues in modeling failure of metallic fuels using peridynamic correspondence model, the PI focused on developing scheme to handle shape tensor singularity and new bond-based failure criterion. The shape tensor singularity was checked before being used in the material model. Whenever singularity is detected, the corresponding bond is considered as broken, which is similar to determined using failure criterion. Some issues still exist with current implementation of this scheme, such as solver nonconvergence in problems with excessive material failure. Investigation is still ongoing to develop valid scheme to handle shape tensor singularity in an implicit solver. For bond-based failure criterion, axial strain for a bond calculated from the strain tensors at the two end material particles was used. Different from critical stretch failure criterion, bond axial strain model can separate the elastic bond strain from the total strain including creep and other

---

[*] Assistant Professor, Department of Mechanical Engineering, University of Kentucky, Lexington, KY 40506

[†] Scientist, Los Alamos National Laboratory, Los Alamos, NM 87545

eigenstrains of an inelastic material. Other creep-damage based failure criterion can also be developed, which will be the future work.

Modeling Metallic Fuel using Peridynamics
Hailong Chen‡ and Cetin Unal§

1. Introduction

Metallic nuclear fuels exhibit extremely complex behavior during irradiation which include but are not limited to thermal expansion, swelling due to gas and solid products of nuclear fission, phase transformation, creep and plastic flow, damage and cracking. Swelling is an especially complex process starting from the production of fission gas atoms, migration, coalescence and release as is well documented in Olander [1] (see Table 13.1). Among the hundreds of fission products, gases such as xenon and krypton, due to their low solubility in the fuel and high yield, precipitate as bubbles. As these gas-filled voids in the fuel expand over time due to diffusion of gas atoms, they contribute to a decrease in the strength of the material and possibly leads to formation of microscale damage and cracks (see **Figure 1**).
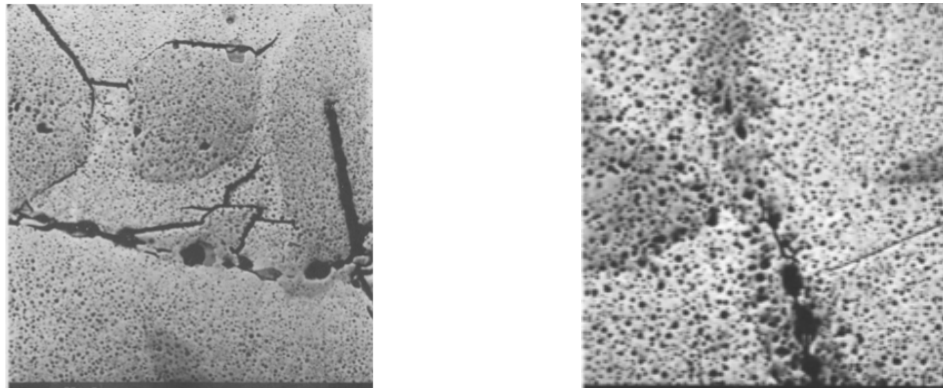

Figure 1. Gas bubble morphology in the intermediate, low-Zr, zone of U-19Pu-10Zr fuel at 3 at. pct burnup % [2].

In addition, cracks can also initiate at the outer surface of the fuel which break the protective zirconium rind which forms as a by-product of fabrication that covers the fuel thereby providing sites for fuel-cladding chemical interactions (see **Figure 2**). In general, these mechanisms are highly dependent on many factors such as composition, temperature, phase, constituent redistribution. For example, the addition of plutonium appears to increase diffusion, decrease strength and accelerate swelling near the high temperature center region [3]. The early onset of rapid swelling in ternary fuels combined with high hoop stresses in the cooler outer regions may promote faster and larger crack growth as compared to binary UZr fuels (see **Figure 2**). Nevertheless, details about the timing, frequency and morphology of cracks are only best estimates from available data and are still a matter of ongoing research.

The literature concerning computational modeling of swelling and swelling induced damage in metallic fuels is rather limited. Information on steady-state metallic fuel codes can be found in Karahan [4]. Some fracture behavior has been simulated in nuclear fuels

---

‡ Assistant Professor, Department of Mechanical Engineering, University of Kentucky, Lexington, KY 40506

§ Scientist, Los Alamos National Laboratory, Los Alamos, NM 87545

using finite elements with a smeared crack model [5]–[7], cohesive zone models [8], peridynamics (PD) [9]–[13], the discrete element method [14] and extended finite element method (XFEM) [15], however these analyses have mostly been limited to oxide fuels.
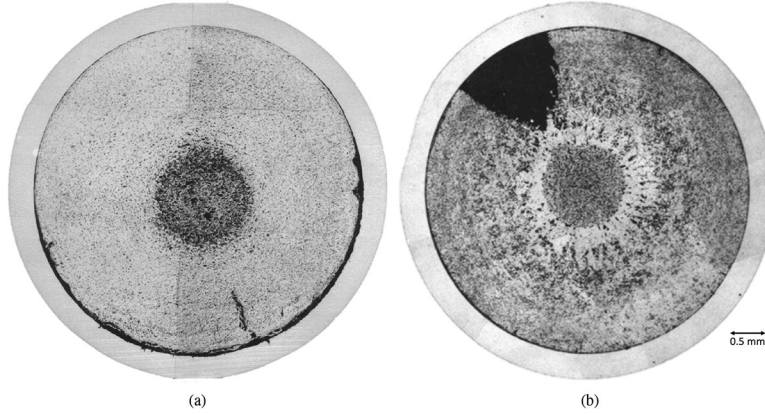
Figure 2. Micrographs of cracks in (a) U-10Zr at 7.3 at. % and (b) U-19Pu-10Zr at 2 at. % showing a late formation of smaller cracks in binary fuels as opposed to early formation of large wedge cracks in ternary fuels [2], [3].

Given the many problems associated with simulating damage and fracture with traditional finite elements, there has been a push to develop other techniques either in conjunction with existing finite element theory such as the XFEM or alternative theories such as PD. Currently, both XFEM and PD are being implemented and tested within the MOOSE multiphysics framework.

PD has been used to simulate nuclear fuel behavior with some promising results [9]–[13], however these analyses have been limited to oxide fuels which are relatively brittle and the effects of creep, plasticity and swelling can be ignored. **Figure 3** shows the temperature, radial displacement and damage obtained from the PD simulation of a UO_2 fuel pellet at the end of the power ramp by Hu et al. [11]. As can be seen, PD is able to capture highly complex crack paths with multiple instances of crack branching as well as coalescence without resorting to any ad-hoc techniques.

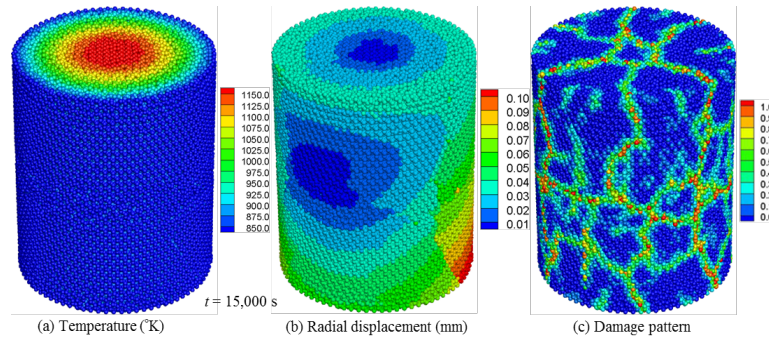
(a) Temperature (°K)   (b) Radial displacement (mm)   (c) Damage pattern

Figure 3. Temperature, radial displacement, and damage pattern obtained from the PD thermomechanical simulation of a UO_2 fuel pellet at the end of power ramp [11].

While peridynamics has been used in the past to model the response of oxide fuels making suitable assumptions that inelastic effects of plasticity, creep, swelling etc. can be ignored, however the same cannot be said for metallic fuels. Swelling causes a high amount of strain and porosity, and creep helps in relaxing the stress, all of which affect the overall behavior of the fuel. Therefore, these inelastic effects are crucial to obtain an accurate solution. Based on current available modeling and simulation capabilities of peridynamics module in MOOSE framework for oxide fuel, the overall goal of this study is to demonstrate the peridynamics capabilities for modeling of metallic nuclear fuels.

The remainder of this work is organized as follows: First, the peridynamic models used in this study is outlined with some details. Following this, material models specific for metallic UPuZr fuel from BISON [16], [17] are briefly discussed and listed. Some details on additional development for modeling both mechanical and thermal contact between fuel and inner cladding surface using peridynamics are discussed. Next, numerical study is performed first to verify the prediction accuracy of peridynamics for metallic fuel in a more practical setup. Some results regarding modeling metal fuel failure using peridynamics are also provided. Conclusion and future work are given at the end.

2. About Peridynamics

Peridynamics is a reformulation of the classical continuum theory by allowing spatial discontinuities, such as crack, to be exist in the solution domain [18]. In peridynamics, the material domain is considered as a collection of material particles whose interaction with neighboring material particles is nonlocal, i.e., a material particle can interact with neighboring material particles up to certain distance, called horizon. The interaction between material particles also is called as bond. The material particles fall in this interaction horizon are called family. See **Figure 4** for illustration.
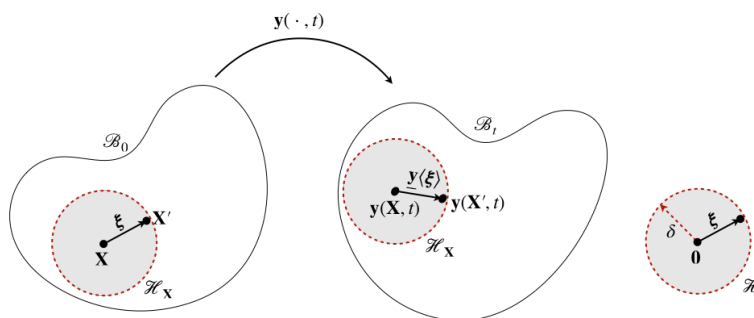
Figure 4. Schematic illustrating some concepts in peridynamics

2.1 Peridynamic mechanics model

For solid mechanics problem, the peridynamic equations of motion have the following general form

$$\rho(X)\ddot{u}(X,t) = \int_{\mathcal{H}_X} f(X,X',t)dV_{X'} + b(X,t) \tag{1}$$

where ρ is mass density, t is time, X and X' are interacting material particles, $\mathcal{H}_X$ is the horizon of material particle X, f is force density function, and u and b are the displacements and body force density vectors.

5

Depending on how the force density function is formulated, peridynamics can be categorized into three distinct model groups: bond-based model, ordinary state-based model, and non-ordinary state-based model. More details about these models can be found in Ref. [18].

One well-known non-ordinary state-based peridynamic model is the correspondence model [19]. This model has the unique capability to incorporate any material constitutive models from the continuum mechanics theory in peridynamic modeling and simulation, which enables modeling any material within the peridynamics framework. The force density of the correspondence model can be written as

$$f(X, X', t) = \underline{T}(X, t) - \underline{T}(X', t) \tag{2}$$

with $\underline{T}$ being the force state, which can be found from the continuum-like stress measures, i.e., the first Piola-Kirchhoff stress tensor P and the shape tensor K, as

$$T(X, t) = \omega P K^{-1} \cdot (X' - X) \tag{3}$$

where ω is a weight function.

The development of the correspondence model was based on the concept of energy equivalency between peridynamics and continuum theory and the formulation of a nonlocal deformation gradient as the weighted least squares error between the deformation state and the reference position vector state [20]. These two states are the differences of the positions between two interacting material particles in the current configuration and the reference configuration (see **Figure 4**), i.e.,

$$\underline{Y} = y' - y \tag{4}$$
$$\underline{X} = \xi = X' - X \tag{5}$$

The nonlocal deformation gradient has the following form

$$F = k \cdot K^{-1} \tag{6}$$

with

$$k = \int_{H_X} \omega \underline{Y} \otimes \underline{X} dV_{X'} \tag{7}$$

and shape tensor

$$K = \int_{H_X} \omega \underline{X} \otimes \underline{X} dV_{X'} \tag{8}$$

Although the correspondence model can directly uses continuum material constitutive models, it suffers from some practical issues, such as formulation instability [20], [21] and fracture instability, which are related to the formulation of the nonlocal deformation gradient. The formulation instability can be understood as for a given force state, there are nonunique set of deformation states within a material particle family which will results in the same force state. A manifestation of this formulation instability is existence of zero-energy modes in the displacement field. The fracture instability is a direct result of violation of the requirement for an invertible shape tensor. During fracture process, the requirement on minimum number of interacting bonds associated at a material particle will not be fulfilled such that the shape tensor will become singular.

For fracture modeling and simulation, bond-based failure criterion has been widely used in peridynamics. A bond is considered as broken hence cannot sustain any force thereafter when a bond-based quantity of interest such as stretch exceeds its critical value. Crack

initiation and growth are the natural outcome of successive bond breakage. A general bond-based failure criterion can be written in terms of a bond status parameter μ as

$$\mu(\boldsymbol{X}, \boldsymbol{X'}, t) = \begin{cases} 1, & s < s_c \\ 0, & otherwise \end{cases} \quad (9)$$

For brittle materials, the critical stretch can be found from the critical energy release rate as [22]

$$S_c = \begin{cases} \sqrt{\dfrac{\pi G_c}{3K\delta}} & 2D \\ \sqrt{\dfrac{5G_c}{9K\delta}} & 3D \end{cases} \quad (10)$$

For materials with inelastic deformation, such as plasticity and creep, the critical stretch failure criterion is problematic and cannot be used [23]. Other failure criterion needs to be developed.

2.2 Peridynamic heat transfer model

Similar to the peridynamic mechanics model, the peridynamic heat transfer model replaces the spatial differential term in the balance equation of continuum heat transfer equation using a nonlocal integral term, which has the following form [24]

$$\rho(\boldsymbol{X})C\dot{T}(\boldsymbol{X}, t) = \int_{\mathcal{H}_X} \boldsymbol{f}(\boldsymbol{X}, \boldsymbol{X'}, t)dV_{X'} + q(\boldsymbol{X}, t) \quad (11)$$

where C is specific heat, T is temperature, and q is heat source/sink.
The thermal response function $\boldsymbol{f}$ is expressed as

$$\boldsymbol{f}(\boldsymbol{X}, \boldsymbol{X'}, t) = k(\boldsymbol{X}, \boldsymbol{X'}) \cdot \frac{T(\boldsymbol{X'}, t) - T(\boldsymbol{X}, t)}{|\boldsymbol{X'} - \boldsymbol{X}|} \quad (12)$$

with the micro-conductivity derived in terms of material conductivity as [11]

$$k(\boldsymbol{X}, \boldsymbol{X'}) = \frac{D\lambda}{|\boldsymbol{X'} - \boldsymbol{X}|} \left(\frac{\sum_{m=1}^{N} V(X_m) + \sum_{n=1}^{N} V(X_n)}{\sum_{m=1}^{N} V(X_m) \sum_{n=1}^{N} V(X_n)} \right) \quad (13)$$

where D is the problem dimensionality, λ is material conductivity, N is the number of material particles within the family, and V is the volume of a material particle.

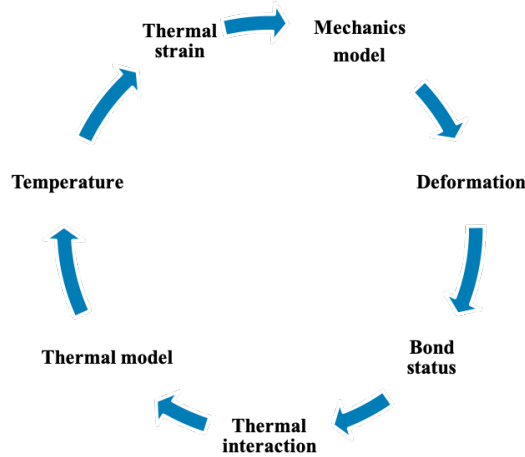*2.3 Coupled peridynamic thermomechanical model*

Figure 5. Two-way coupling in peridynamic thermomechanical model

A two-way coupled peridynamic thermomechanical model was developed based on aforementioned peridynamic mechanics and thermal models [12]. The basic idea is that the thermal model will contribute thermal eigenstrain to the mechanics model as a driving force, while the mechanics model determines the status of a bond which in turn will affect the heat transfer between material particles in the thermal model. A schematic depicting this two-way coupling is shown in **Figure 5**.

3. Material models

Some material models used in this work are presented in this section. The corresponding material class names in BISON while compiling this work is also reported. More details about these material models can be found in the BISON documentation system [25].

3.1 Fuel burn up model (UPuZrBurnup)

Burnup is used to calculate fuel properties and the fuel densification and swelling rate. It is calculated based on the following equation from [1]

$$\beta = \frac{\dot{F}t}{N_f^0} \tag{14}$$

where $\dot{F}$ is the volumetric fission rate, t is time, and N_f^0 is the initial density of heavy metal atoms in the fuel.

3.2 Fuel elasticity tensor model (UPuZrElasticityTensor)

The Young's modulus and Poisson's ratio of metal fuel has following general form [26]

$$E = 1.6 \times 10^{11}(1 - D_E p)\left(\frac{1 + 0.17w_{Zr}}{1 + 1.34w_{Zr}} - w_{Pu}\right)E_T \tag{15}$$

$$E_T = \left(1 - \frac{1.06(T - 588)}{1405} - 0.3\left(1 - \frac{1.06(T_\alpha - 588)}{T_{mU}}\right)S_\alpha\right) \tag{16}$$

$$v = 0.24(1 - D_v p)\left(\frac{1 + 3.4w_{Zr}}{1 + 1.34w_{Zr}} - w_{Pu}\right)\left(1 + \frac{1.2(T_\alpha - 588)}{1405}\right) \tag{17}$$

where D is degradation parameter, p is porosity, and S_α is a smoother function depending in the current temperature, starting and ending temperatures of α-phase transition.

3.3 Fuel creep model (UPuZrCreepUpdate)

A combined secondary thermal creep and irradiation creep for U-Pu-Zr fast reactor fuel is taken from Kutty et al. [27], and is given as

$$\dot{\varepsilon}_{cr} = A_1(1 + 7.9p + 470p^2)e^{-\frac{Q_1}{RT}}\bar{\sigma} + A_2(1 - p^{0.67})^{-4.5}e^{-\frac{Q_2}{RT}}\bar{\sigma}^{4.5} + A_3\dot{F}\bar{\sigma} \tag{18}$$

where $A_1 = 5 \times 10^3$, $A_2 = 6$, $A_3 = 7.7 \times 10^{-23}$, $Q_1 = Q_2 = 52000$ Cal/mol, $R = 1.987$ Cal/mol-K, T is temperature, p is porosity, $\dot{F}$ is volumetric fission rate, $\bar{\sigma}$ is effective stress.

These U and Pu alloys have a phase change temperature of 923.15 K. Above this temperature, the creep rate equation changes to

$$\dot{\varepsilon}_{cr} = A_4(1 - p^{0.67})^{-3}e^{-\frac{Q_3}{RT}}\bar{\sigma}^3 + A_3\dot{F}\bar{\sigma} \tag{19}$$

where $A_4 = 8.0 \times 10^{-2}$ and $Q_3 = 28500$ Cal/mol.

The negative strain component due to the compression of open pores is also calculated as [28]

$$\left(\frac{\Delta V}{V_0}\right)_{pore} = 9\alpha_c\left(\sigma_r + \sigma_\theta + \sigma_z + 3P_p\right)\frac{\varepsilon_c^{eq}}{\sigma^{eq}} \tag{20}$$

where α_c is open pore compressibility factor, σ^{eq} is modified equivalent stress, P_p is plenum pressure.

3.4 Fuel swelling models (UPuZrGaseousEigenstrain & BurnupDependentEigenstrain)

The fuel swelling due to fission gas is obtained as

$$\left(\frac{\Delta V}{V_0}\right)_g = \frac{3.59 \times 10^{-24} FT}{1.01 \times 10^7 - \sigma_h} \tag{21}$$

where σ_h is hydrostatic stress.
The fuel swelling due to solid fission products is assumed to be 1.5% per 1% burnup as suggested by [29]

$$\left(\frac{\Delta V}{V_0}\right)_s = 4.16 \times 10^{-29} F \tag{22}$$

The porosity of metal fuel is obtained as

$$p = \frac{\left(\frac{\Delta V}{V_0}\right)_g}{\left(\frac{\Delta V}{V_0}\right)_g + 1} \tag{23}$$

3.5 Fuel thermal conductivity (ThermalUPuZr)

The thermal conductivity of the fuel is given as [30], [31]

$$k_{U-Pu-Zr} = \left(1 - \sqrt{1 - w_{Pu}}\right)k_{Pu} + \sqrt{1 - w_{Pu}}\left[(1 - w_{Pu})k_{U-Zr} + w_{Pu}k_{c,Pu}\right] \tag{24}$$

with

$$w_{Pu} = xA_{Pu}/\left((1 - x - y)A_U + xA_{Pu} + yA_{Zr}\right) \tag{25}$$

$$w_{Zr} = yA_{Zr}/\left((1 - x - y)A_U + xA_{Pu} + yA_{Zr}\right) \tag{26}$$

$$w_U = (1 - x - y)A_U/\left((1 - x - y)A_U + xA_{Pu} + yA_{Zr}\right) \tag{27}$$

where x and y are the weight fractions of Pu and Zr, respectively, A is the atomic weight of each element,

$$k_{Pu} = -8.162 + 4.841 \times 10^{-2}T - 1.614 \times 10^{-5}T^2 \tag{28}$$

$$k_{U-Zr} = \left(1 - \sqrt{1 - f_{Zr}}\right)k_{Zr} + \sqrt{1 - f_{Zr}}\left(f_{Zr}k_{c,U-Zr} + (1 - f_{Zr})k_U\right) \tag{29}$$

where the adjusted weight function

$$f_{Zr} = w_{Zr}/(w_{Zr} + w_U) \tag{30}$$

$$k_U = 21.73 + 1.591 \times 10^{-2}T + 5.907 \times 10^{-6}T^2 \tag{31}$$

$$k_{Zr} = 8.853 + 7.082 \times 10^{-3}T + 2.533 \times 10^{-6}T^2 + 2.992 \times 10^3 T^{-1} \tag{32}$$

$$k_{c,U-Zr} = -102 - 200.1f_{Zr} - 109.2f_{Zr}^2 + 9.435 \times 10^{-3}T + 3.459 \times 10^{-5}T^2 \\ - 0.02093f_{Zr}T \tag{33}$$

$$k_{c,Pu} = -135.8 - 29.89w_{Pu} + 351.9w_{Pu}^2 + 0.3571 - 1.186 \times 10^{-4}T^2 - 0.961w_{Pu}T \tag{34}$$

3.6 Clad creep model (HT9CreepUpdate)

The thermal and irradiation creep models and material properties from [26] are used for the clad creep model. The effective thermal and irradiation creep strain rate for the secondary creep is calculated as

$$\dot{\varepsilon}_{cr} = C_5 e^{-\frac{Q_4}{RT}}\bar{\sigma}^2 + C_6 e^{-\frac{Q_5}{RT}}\bar{\sigma}^5 + \left[B_0 + Ae^{-\frac{Q}{RT}}\right]\phi\bar{\sigma}^{1.3} \tag{35}$$

9

where $C_5 = 1.17 \times 10^9$, $C_6 = 8.33 \times 10^9$, $Q_4 = 83142$ Cal/g-mol, $Q_5 = 108276$ Cal/g-mol, $B_0 = 1.83 \times 10^{-4}$, $A = 2.59 \times 10^{14}$, $Q = 73000$ Cal/g-mol, $R = 1.987$ Cal/g-mol, T is temperature, ϕ is neutron flux, $\bar{\sigma}$ is effective stress.

3.7 Clad thermal conductivity (ThermalHT9)

The thermal conductivity is temperature dependent and calculated as [32]

$$k = \begin{cases} 17.622 + 2.42 \times 10^{-1}T - 1.696 \times 10^{-5}T^2, & T < 1030 \text{ K} \\ 12.027 + 1.218 \times 10^{-2}T, & x \geq 1030 \text{ K} \end{cases} \tag{36}$$

4. Contact models

The enforcement of both mechanical and thermal contact conditions in peridynamics is based on available algorithms developed for FEM in the MOOSE framework. Fictitious triangular elements (2D) or tetrahedral (3D) are constructed based on peridynamic material particles located at the interface where contact is expected. Side sets of fictitious elements are used to enforce the contact constraints. See **Figure 6**.
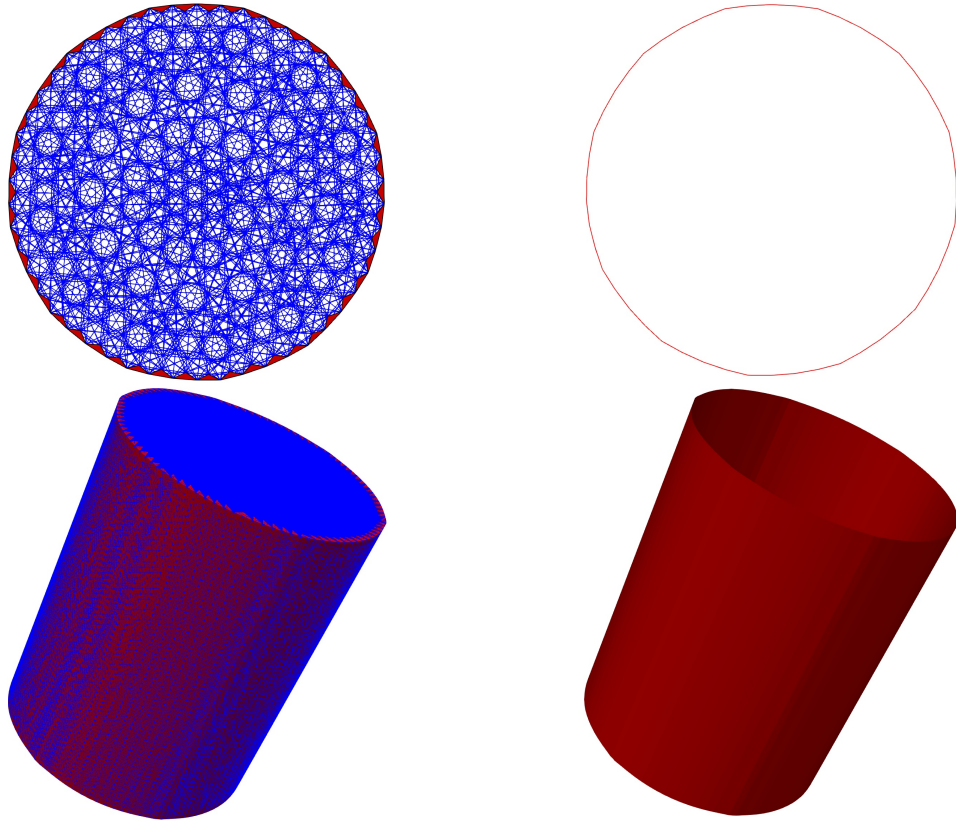

Figure 6. Fictitious finite elements and side sets constructed from peridynamic material particles for 2D circular and 3D cylindrical geometries

Since peridynamics considers the deformation of a material particle only at its center, an offset is provided to account for the actual contact occurs at the perimeter of a material particle rather than at its center. This offset value can be calculated when converting finite element mesh to peridynamic mesh. For completeness, some details about contact models in MOOSE are also provided below.

4.1 Mechanical contact model

The mechanical contact between two surfaces (fuel and inside surface of the cladding) is based on three requirements:

$$g \leq 0 \tag{37}$$
$$t_N \geq 0 \tag{38}$$
$$t_N g = 0 \tag{39}$$

That is, the penetration distance or gap g of one body into another must not be positive; the contact force t_N opposing penetration must be positive in the normal direction; and either the penetration distance or contact force must be zero at all times.

In MOOSE, these constraints are enforced through the use of node/face constraints. Specifically, the nodes of the fuel are prevented from penetrating cladding faces.

4.2 Gap heat transfer model

Thermal contact between two surfaces is modeled using the gap heat transfer model as

$$h_{gap} = h_g + h_s + h_r \tag{40}$$

where h_{gap} is the total conductance across the gap, h_g is the gas conductance, h_s is the pressure-dependent increased conductance due to solid-solid contact, and h_r is the conductance due to radiant heat transfer. The above conductance are given below:

$$h_g = \frac{k_g(T_g)}{d_g + C_r(r_1 + r_2) + g_1 + g_2} \tag{41}$$

where k_g is the conductivity of the gas in the gap, d_g is the gap width, C_r is a roughness coefficient with r_1 and r_2 the roughness of the two surfaces, and g_1 and g_2 are jump distances at the two surfaces. The gas temperature T_g is taken as an average of the temperature of all solid surfaces in contact with the gas.

$$h_s = C_s \frac{2k_1 k_2}{k_1 + k_2} \frac{P_C}{\delta^{1/2} H} \tag{42}$$

where C_s is a constant (typically 1.0), k_1 and k_2 are the thermal conductivities of the solid materials in contact, P_C is the contact pressure, δ is the average gas film thickness, and H is the Meyer hardness of the softer material.

$$h_r = \sigma F_e (T_1^2 + T_2^2)(T_1 + T_2) \tag{43}$$

where σ is the Stephan-Boltzmann constant, T_1 and T_2 are the temperatures of the radiating surfaces, and the emissivity function F_e of the emissivitives ε_1 and ε_2 of the radiating surfaces as

$$F_e = \frac{1}{1/\varepsilon_1 + 1/\varepsilon_2 - 1} \tag{44}$$

5. Numerical results

In this section, we present the numerical results obtained using the developed peridynamics capability based on the MOOSE framework. A radial cross section of a metallic fuel pin from the EBR-II x441 experiments is modeled by assuming plane strain condition. The schematics of the geometric models, and the meshes for finite element model and finite element-peridynamics model are shown in **Figure 7**. The focus is to model the fuel behavior under power ramping and constant power state. Therefore, peridynamics is employed only to model the fuel and finite element model is used for the cladding. Input parameters including the dimensions of the cross section are given in **Table 1**.

Table 1. Input parameters for the plane strain problem

Fuel radius (mm)	2.195
Clad inner radius (mm)	2.54
Clad outer radius (mm)	2.92
Clad Young's modulus (GPa)	1.88
Clad Poisson's ratio	0.236
Clad thermal expansion coefficient (K^{-1})	1.2×10^{-5}
Fast neutron flux ($n/m^2 s$)	2.47×10^{19}
Fuel thermal expansion coefficient (K^{-1})	1.18×10^{-5}
Energy per fission constant ($J/fission$)	3.28451×10^{-11}
Weight fraction of Pu	0.163
Weight fraction of Zr	0.225

The boundary conditions are heat source due to fission at the fuel cross-sectional area, and prescribed temperature profile at the cladding outer circumference due to coolant flow, which are obtained from an axisymmetric model in BISON. The fission rate and temperature profiles from axisymmetric analysis using BISON are shown in **Figure 8**. To fully constrain both the fuel and the cladding, displacement boundary conditions are imposed to allow the horizontal nodes/material particles and the vertical nodes/material particles to deform horizontally and vertically, respectively. The total run time is 1.5×10^7 seconds.

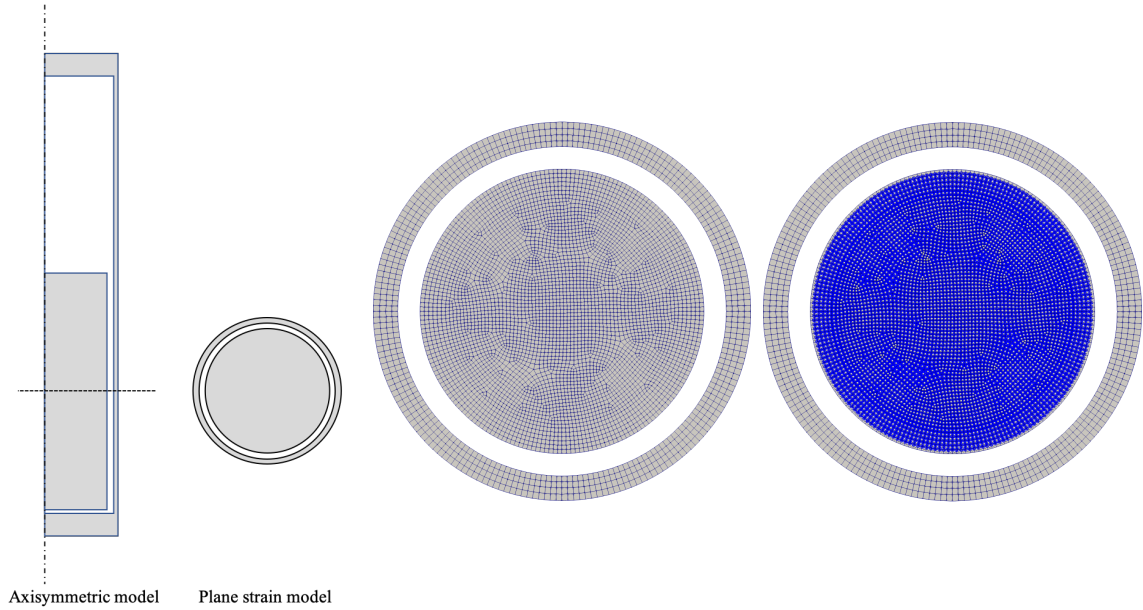Axisymmetric model   Plane strain model

Figure 7. 2D geometric models for a typical EBRII-x441 fuel pin. (left) Axisymmetric model and corresponding cross section for plane strain model. (middle) Finite element mesh. (right) Finite element mesh for cladding and peridynamic mesh for fuel (gray dots indicate material particles and blue lines indicate bonds).

Two different discretization densities are used for the fuel. For mesh density case 1, there are total 200 nodes along the fuel, clad inner, and clad outer peripheries, which results in a

total of 4,540 finite elements for fuel and 800 finite elements for cladding. After converting finite elements to peridynamic material particles for the fuel region, there are total 64,377 peridynamic bonds. The average gap offset of the fuel represented using peridynamic material particles for mesh density 1 is 0.033 mm. For mesh density case 2, 300 nodes were used for the fuel perimeter. The node densities for cladding are kept the same. This results in a total of 9,081 finite elements for fuel, and 127,364 peridynamic bonds after the mesh conversion. The average gap offset value for mesh density 2 is 0.02 mm.
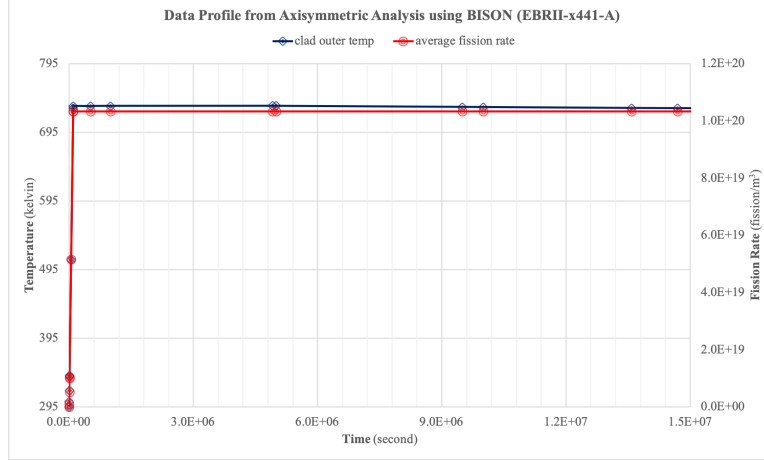

Figure 8. The fission rate and temperature profiles from axisymmetric analysis using BISON.

5.1 Deformation verification

We first verify the prediction accuracy of the peridynamic thermomechanical model for deformation problem against finite element solution. To handle the formulation instability of the peridynamic correspondence mechanics model, method based on bond-associated horizon can be used [20], [21]. In this study, a new weight function stabilization method is used. The details about this method will be presented in future publication.

To study the discretization density effect on the prediction accuracy in peridynamics, the results obtained using the two meshes are compared to finite element results. The comparisons of temperatures at the fuel center and clad inner perimeter are shown in **Figure 9** and **Figure 10**, respectively. The comparison of radial displacements at the clad inner perimeter is shown in **Figure 11**.
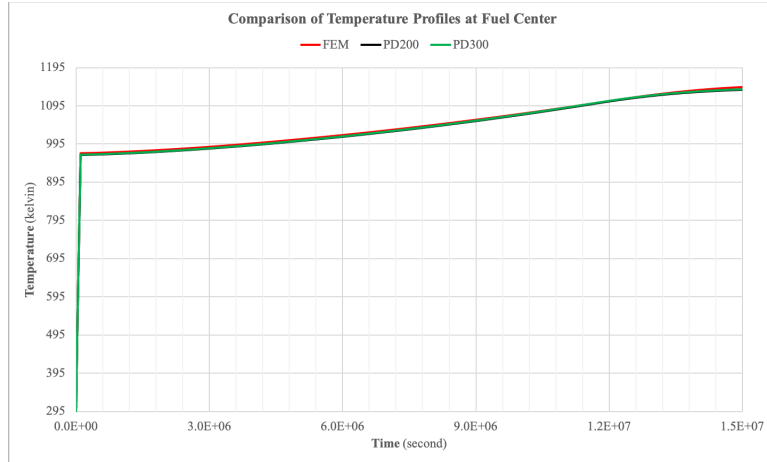
Figure 9. Comparison between FEM and PD predictions of temperature profile at the fuel center.
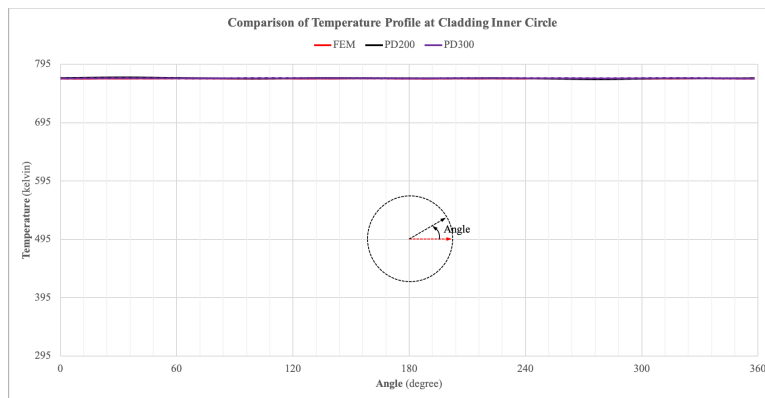

Figure 10. Comparison between FEM and PD predictions of temperature at the clad inner perimeter.
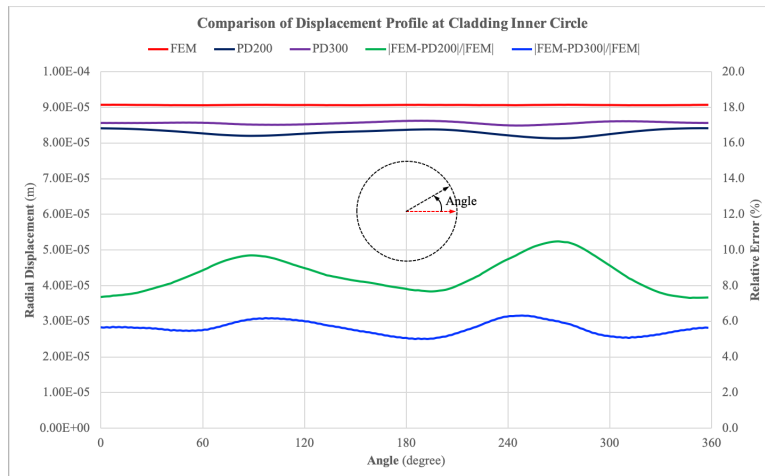

Figure 11. Comparison between FEM and PD predictions on radial displacement at the clad inner circumference.

As can be seen from **Figure 9** and **Figure 10**, both meshes give very good predictions as compared to finite element solution, which indicates the validity of the gap heat transfer model using fictitious finite elements and the prediction accuracy of the peridynamic thermal model. For radial displacement comparison shown in **Figure 11**, the relative difference between peridynamics prediction and finite element solution is within 10.5% and 6.5% for mesh case 1 and case 2, respectively. The improvement in the prediction is linearly related to the increase of mesh density. Another source of error in the peridynamics prediction is the gap offset. The material within the offset region is assumed rigid and no deformation, which decreases the compression from the fuel on the clad inner perimeter, hence reduces the radial displacement of the clad inner perimeter. The skin or free surface effect which is a well-known issue in peridynamic may also contribute to this difference. Further study is needed to improve the prediction accuracy of peridynamics for mechanical contact problems.

For the rest of deformation verification, only the results using mesh case 2 are presented. The comparison of the temperature field of the whole fuel pin cross section is shown in **Figure 12**. The comparisons of the temperature and radial displacement fields with contour lines for the fuel cross section are shown in **Figure 13** and **Figure 14**, respectively.
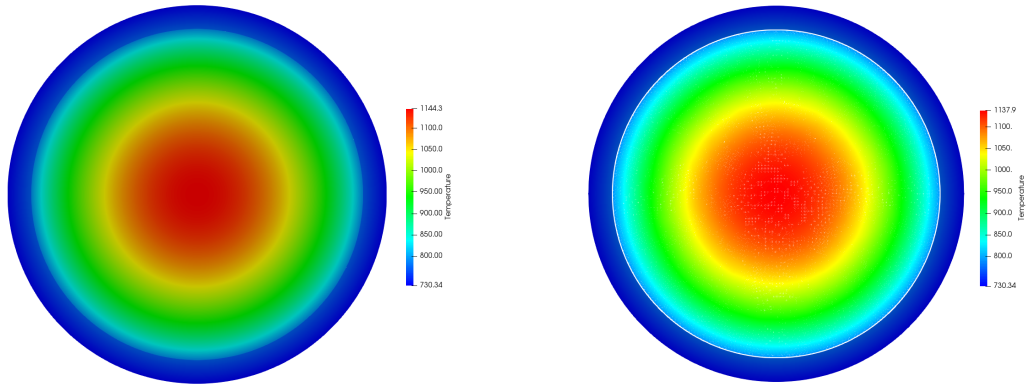

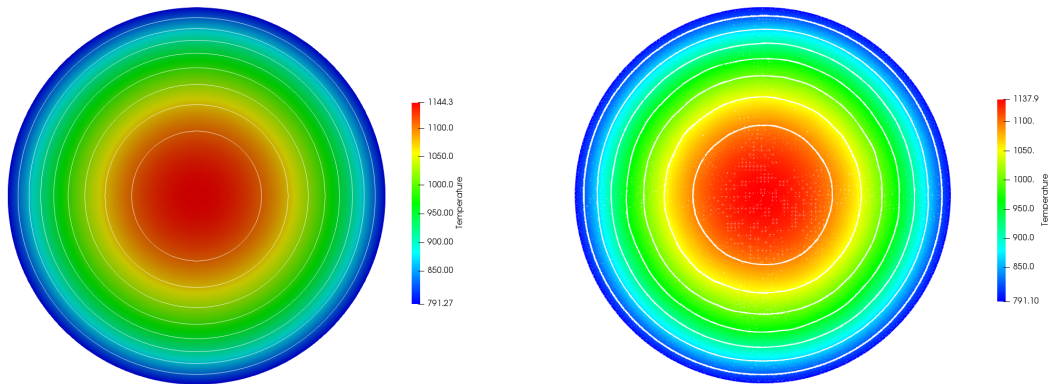**Figure 12.** Comparison between FEM (left) and PD (right) predictions on temperature of the fuel pin.

Figure 13. Comparison between FEM (left) and PD (right) predictions on temperature of the fuel.
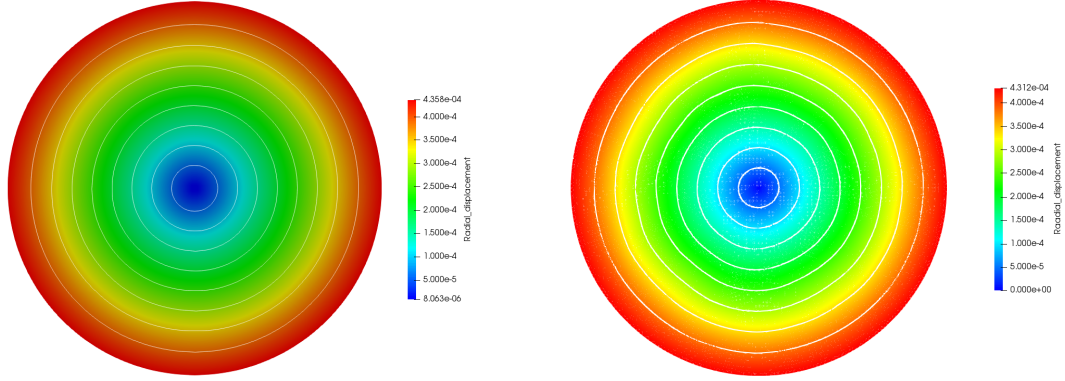
Figure 14. Comparison between FEM (left) and PD (right) predictions on radial displacement of the fuel.

The temperature field comparison shown in **Figure 12** and **Figure 13** further establish the validity and accuracy of the gap heat transfer model and thermal model in peridynamics. From **Figure 14**, it can be seen that peridynamics predicts very accurate radial displacement field for the fuel cross section, as compared to finite element result. The slight differences in the prediction of both the temperature and radial displacement are resulted from the fact that relatively smaller cross section of the fuel is modeled in peridynamics compared to that modeled using the finite element method.

The comparison of the von Mises stress and the creep strain components xx and yy are shown in **Figure 15** and **Figure 16**, respectively. For the von Mises stress comparison, two different legends are used to scale the same result, one is based on the finite element prediction and the other is the actual peridynamics prediction.
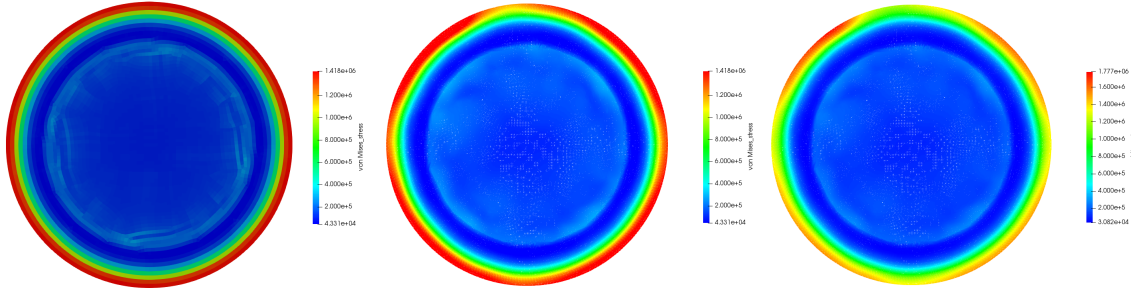

Figure 15. Comparison between FEM (left) and PD (middle and right) predictions on von Mises stress of the fuel.

As can be seen in **Figure 15**, the predicted von Mises stress field using peridynamics is good agreement with the finite element solution, expect the difference in predicted maximum and minimum values. For the creep strain predictions in **Figure 16**, the predicted contour using peridynamics is slightly different for the results using finite element method. The peridynamics results shows some mesh dependency in creep strain prediction. This is also a potential source results in discrepancy in the radial displacement at the clad inner perimeter presented in **Figure 11**. Further investigation is needed.
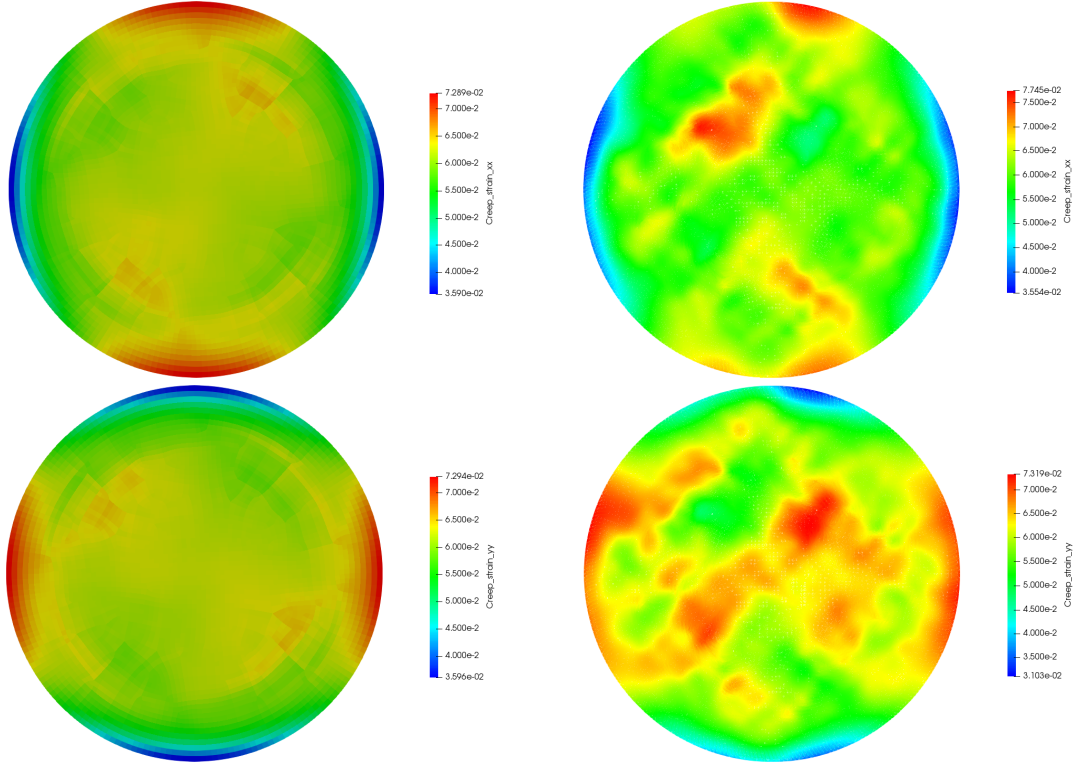
Figure 16. Comparison between FEM (left) and PD (right) predictions on creep strains of the fuel.

5.2 Failure prediction

To handle the fracture instability of the peridynamic correspondence mechanics model, the deformation gradient of a bond whose bond-associated shape tensor is singular is set to unity and the corresponding bond is treated as broken. Therefore, whenever a bond has singular shape tensor, it is treated as broken, similar to determined using bond failure criterion. The validity of this treatment needs additional study.

To model bond failure, elastic strain-based failure criterion is used in this study. Different from the bond stretch criterion, the axial strain along the bond direction is calculated based on the strain tensors of the two material particles connected by the bond, which can be expressed as

$$e^{bond} = \frac{1}{2}\left(\varepsilon_{ij}^{(1)} + \varepsilon_{ij}^{(2)}\right)n_i^{bond}n_j^{bond} \tag{45}$$

where $\boldsymbol{n}$ is the bond direction.

This axial strain calculation allows the separation of elastic strain from other strains due to creep and volumetric expansion. It also can be applied to other strain tensors such as creep strain to study their effect on material failure. The critical elastic axial strain used is 0.03% with a standard deviation of 0.001% to represent a non-uniform distribution of material strength across the whole fuel cross section. These values don't have any physical meaning rather than generating critical values of bonds to quantitatively model the fuel failure

behavior. The failure predictions at various simulation time are shown in **Figure 17**. The total run time for this example is 6585580 seconds.
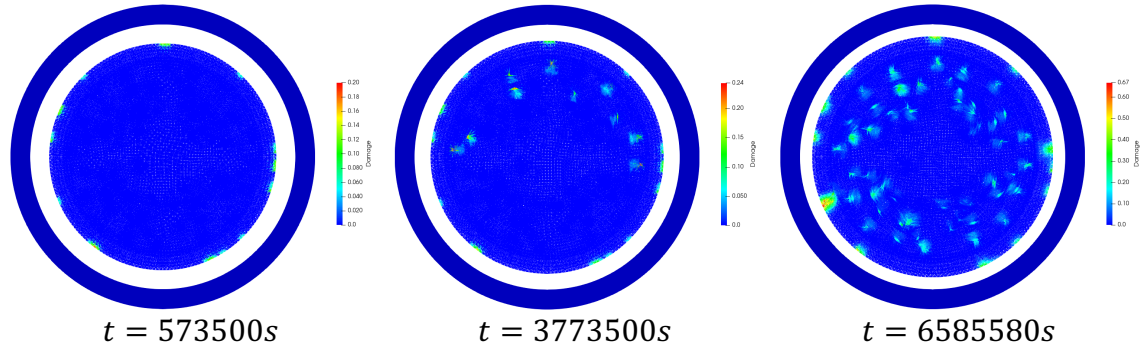

| $t = 573500s$ | $t = 3773500s$ | $t = 6585580s$ |

Figure 17. Failure pattern predicted using peridynamics at different simulation time.

As can be seen from the results shown in **Figure 17**, the material failure initiates at the fuel perimeter due to excessive expansion of the fuel at the beginning of the simulation. With the increase of temperature and simulation time, internal material starts to fail with the increase of creep strain at the fuel inside region. Further fuel expansion makes the damage initiated at the fuel perimeter to propagate, with the formation of major cracks towards the fuel center. Due to the current way of handling the shape tensor singularity, solver abruptly stopped at time of 6585580 seconds. Research is ongoing to solve this issue to run the simulation to completion.

6. Conclusion and future work

In this work, peridynamics was applied to model the metallic fuel under power ramping and constant power state for the first time. For a more realistic study, experimental data-based material models from BISON were used, including creep models and temperature- and phase-dependent material properties for both fuel and cladding, and burnup and swelling models for the fuel. Some details on modeling mechanical and thermal contact within the framework of peridynamics were discussed. For numerical study, a radial cross section of an EBR-II x441 fuel pin was modeled under the plane strain condition, in which the fuel was modeled using peridynamics while the cladding was modeled using finite elements. Temperature and fission rate boundary conditions were obtained from an axisymmetric analysis using BISON. For verifying the prediction accuracy of peridynamics for deformation problems, the peridynamics results were first compared against with finite element model. A mesh convergence study was performed to use two different mesh densities for the peridynamic model. Good agreements between peridynamics predictions and finite element results were observed. The peridynamic model was then applied to model the failure of metallic fuel. The same setup as the deformation problem but considering material failure was used. An elastic strain-based failure criterion was used. The elastic strain-based failure criterion predicted the failure starts at the fuel perimeter due to excessive expansion of the fuel. Internal material failure was also predicted as the increase of creep strain at the fuel center region.

Future work is to improve the current peridynamic models and perform systematic study on failure modeling of metallic fuel, such as the effects of initial defects, voids, phase contents, and the temperature and stress gradients on the damage initiation and growth.

Acknowledgement

References

[1]   D. R. Olander, "Fundamental aspects of nuclear reactor fuel elements: solutions to problems," U.S. Department of Energy, Jan. 1976.

[2]   G. L. Hofman, R. G. Pahl, C. E. Lahm, and D. L. Porter, "Swelling behavior of U-Pu-Zr fuel," *Metall. Trans. A*, vol. 21, no. 2, pp. 517–528, Feb. 1990.

[3]   C. Matthews, C. Unal, J. Galloway, D. D. Keiser, and S. L. Hayes, "Fuel-cladding chemical interaction in U-Pu-Zr metallic fuels: A critical review," *Nuclear Technology*, vol. 198, no. 3. American Nuclear Society, pp. 231–259, 01-Jun-2017.

[4]   A. Karahan, "Modelling of thermo-mechanical and irradiation behavior of metallic and oxide fuels for sodium fast reactors," Massachusetts Institute of Technology, 2009.

[5]   M. R. Tonks *et al.*, "Mechanistic materials modeling for nuclear fuel performance," *Annals of Nuclear Energy*, vol. 105. Elsevier Ltd, pp. 11–24, 01-Jul-2017.

[6]   N. Marchal, C. Campos, and C. Garnier, "Finite element simulation of Pellet-Cladding Interaction (PCI) in nuclear fuel rods," *Comput. Mater. Sci.*, vol. 45, no. 3, pp. 821–826, May 2009.

[7]   Y. R. Rashid, "Mathematical modeling and analysis of fuel rods," *Nucl. Eng. Des.*, vol. 29, no. 1, pp. 22–32, Nov. 1974.

[8]   R. L. Williamson, "Simulating Dynamic Fracture in Oxide Fuel Pellets Using Cohesive Zone Models," in *SMiRT 20*, 2009.

[9]   S. Oterkus and E. Madenci, "Peridynamic modeling of fuel pellet cracking," *Eng. Fract. Mech.*, vol. 176, pp. 23–37, May 2017.

[10]   R. Mella and M. R. Wenman, "Modelling explicit fracture of nuclear fuel pellets using peridynamics," *J. Nucl. Mater.*, vol. 467, pp. 58–67, Dec. 2015.

[11]   Y. Hu, H. Chen, B. W. Spencer, and E. Madenci, "Thermomechanical peridynamic analysis with irregular non-uniform domain discretization," *Eng. Fract. Mech.*, vol. 197, pp. 92–113, Jun. 2018.

[12]   H. Chen, Y. Hu, and B. W. B. W. Spencer, "A MOOSE-Based Implicit Peridynamic Thermo-Mechanical Model," in *ASME 2016 International Mechanical Engineering Congress and Exposition*, 2016, vol. 9, pp. IMECE2016-65552.

[13]   Y. Wang, X. Zhou, and M. Kou, "Peridynamic investigation on thermal fracturing behavior of ceramic nuclear fuel pellets under power cycles," *Ceram. Int.*, vol. 44, no. 10, pp. 11512–11542, Jul. 2018.

[14]   H. Huang, B. Spencer, and J. Hales, "Discrete element method for simulation of early-life thermal fracturing behavior in ceramic nuclear fuel pellets," *Nucl. Eng. Des.*, vol. 278, pp. 515–528, Oct. 2014.

[15]   W. Jiang, B. W. Spencer, and J. E. Dolbow, "Ceramic nuclear fuel fracture modeling with the extended finite element method," *Eng. Fract. Mech.*, vol. 223, p. 106713, Jan. 2020.

[16]   R. L. Williamson *et al.*, "Multidimensional multiphysics simulation of nuclear fuel behavior," *J. Nucl. Mater.*, vol. 423, no. 1–3, pp. 149–163, Apr. 2012.

[17]   J. D. Hales, S. R. Novascone, B. W. Spencer, R. L. Williamson, G. Pastore, and D. M. Perez, "Verification of the BISON fuel performance code," *Ann. Nucl. Energy*,

vol. 71, pp. 81–90, Sep. 2014.

[18] F. Bobaru, J. T. Foster, P. H. Geubelle, and S. A. Silling, *Handbook of Peridynamic Modeling*. Boca Raton, FL: CRC Press, 2016.

[19] S. A. Silling, M. Epton, O. Weckner, J. Xu, and E. Askari, "Peridynamic States and Constitutive Modeling," *J. Elast.*, vol. 88, no. 2, pp. 151–184, 2007.

[20] H. Chen, "Bond-associated deformation gradients for peridynamic correspondence model," *Mech. Res. Commun.*, Jun. 2018.

[21] H. Chen and B. W. Spencer, "Peridynamic bond-associated correspondence model: Stability and convergence properties," *Int. J. Numer. Methods Eng.*, vol. 117, no. 6, pp. 713–727, Nov. 2019.

[22] S. A. Silling and E. Askari, "A meshfree method based on the peridynamic model of solid mechanics," *Comput. Struct.*, vol. 83, no. 17–18, pp. 1526–1535, 2005.

[23] J. T. Foster, S. A. Silling, and W. Chen, "An Energy based Failure Criterion for use with Peridynamic States," *Int. J. Multiscale Comput. Eng.*, vol. 9, no. 6, pp. 675–688, 2011.

[24] S. Oterkus, E. Madenci, and A. Agwai, "Peridynamic thermal diffusion," *J. Comput. Phys.*, vol. 265, pp. 71–96, 2014.

[25] "Introduction to BISON Theory." [Online]. Available: https://mooseframework.org/bison/theory/introduction.html.

[26] G. L. Hofman, L. Leibowitz, J. M. Kramer, M. C. Billone, and J. F. Koenig, "Metallic fuels handbook," Argonne, IL (United States), Nov. 1985.

[27] T. R. G. Kutty, C. B. Basak, A. Kumar, and H. S. Kamath, "Creep behaviour of δ-phase of U-Zr system by impression creep technique," *J. Nucl. Mater.*, vol. 408, no. 1, pp. 90–95, Jan. 2011.

[28] A. Karahan and J. Buongiorno, "A new code for predicting the thermo-mechanical and irradiation behavior of metallic fuels in sodium fast reactors," *J. Nucl. Mater.*, vol. 396, no. 2–3, pp. 283–293, Jan. 2010.

[29] T. Ogata and T. Yokoo, "Development and validation of ALFUS: an irradiation behavior analysis code for metallic fast reactor fuels," *Nucl. Technol.*, vol. 128, no. 1, pp. 113–123, 1999.

[30] J. Galloway, C. Unal, N. Carlson, D. Porter, and S. Hayes, "Modeling constituent redistribution in U-Pu-Zr metallic fuel using the advanced fuel performance code BISON," *Nucl. Eng. Des.*, vol. 286, pp. 1–17, May 2015.

[31] Y. S. Kim, T. W. Cho, and D. S. Sohn, "Thermal conductivities of actinides (U, Pu, Np, Cm, Am) and uranium-alloys (U-Zr, U-Pu-Zr and U-Pu-TRU-Zr)," *J. Nucl. Mater.*, vol. 445, no. 1–3, pp. 272–280, Feb. 2014.

[32] L. Leibowitz and R. A. Blomquist, "Thermal conductivity and thermal expansion of stainless steels D9 and HT9," *Int. J. Thermophys.*, vol. 9, no. 5, pp. 873–883, Sep. 1988.